UC San Diego

UC San Diego Previously Published Works

Title

Exciton Gas Transport through Nanoconstrictions

Permalink

https://escholarship.org/uc/item/5gh5g222

Journal

Nano Letters, 19(8)

ISSN

1530-6984

Authors

Xu, Chao
Leonard, Jason R
Dorow, Chelsey J
et al.

Publication Date

2019-08-14

DOI

10.1021/acs.nanolett.9b01877

Peer reviewed

eScholarship.org Powered by the California Digital Library
University of California

NANO LETTERS
Letter
Cite This: Nano Lett. 2019, 19, 5373−5379
pubs.acs.org/NanoLett

Exciton Gas Transport through Nanoconstrictions

Chao Xu,*[,†] Jason R. Leonard,[†] Chelsey J. Dorow,[†] Leonid V. Butov,[†] Michael M. Fogler,[†] Dmitri E. Nikonov,[‡] and Ian A. Young[‡]

[†]Department of Physics, University of California, San Diego, 9500 Gilman Drive, La Jolla, California 92093, United States
[‡]Components Research, Intel Corporation, Hillsboro, Oregon 97124, United States

Supporting Information

ABSTRACT: An indirect exciton is a bound state of an electron and a hole in spatially separated layers. Two-dimensional indirect excitons can be created optically in heterostructures containing double quantum wells or atomically thin semiconductors. We study theoretically the transmission of such bosonic quasiparticles through nanoconstrictions. We show that the quantum transport phenomena, for example, conductance quantization, single-slit diffraction, two-slit interference, and the Talbot effect, are experimentally realizable in systems of indirect excitons. We discuss similarities and differences between these phenomena and their counterparts in electronic devices.

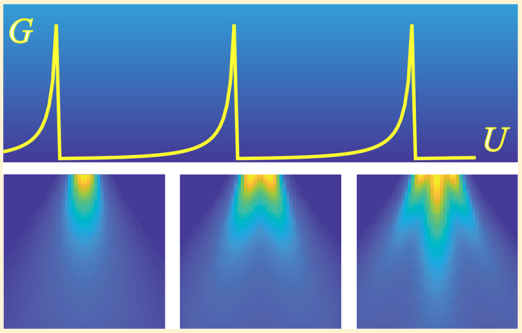

KEYWORDS: *Indirect excitons, quantum point contact, ballistic transport, split gate*

Indirect excitons (IXs) in coupled quantum wells have emerged as a new platform for investigating quantum transport. The IXs have a long lifetime,[1] long propagation distance,[2−9] and long coherence length at temperatures T below the temperature T_0 of quantum degeneracy (eq 7).[10] Although an IX is overall charge neutral, it can couple to an electric field via its static dipole moment ed, where d is the distance between the electron and hole layers (Figure 1a). These properties enable experimentalists to study the transport of quasi-equilibrium IX systems subject to artificial potentials controlled by external electrodes (Figure 1b).

In this Letter, we examine theoretically the transport of IXs through nanoconstrictions (Figure 1c−e).[11] Historically, studies of transmission of particles through narrow constrictions have led to many important discoveries. In particular, investigations of electron transport through so-called quantum-point contacts (QPCs) have revealed that at low T, the conductance of smooth, electrostatically defined QPCs exhibits a step-like behavior as a function of their width.[12,13] The steps appear in integer multiples of Ne^2/h (except for the anomalous first one)[14] because the electron spectrum in the constriction region is quantized into one-dimensional (1D) subbands (Figure 2e), where N is the spin-valley degeneracy. Associated with such subbands are current density profiles analogous to the diffraction patterns of light passing through a narrow slit. These patterns have been observed by nanoimaging of the electron flow.[15] The conductance quantization has also been observed in another tunable Fermionic system, a cold gas of ^{6}Li atoms.[16]

For the transport of bosonic IXs, we have in mind a conventional in solid-state physics setup where the QPC is connected to the source and drain reservoirs of unequal electrochemical potentials, ζ_s and ζ_d [Figure 2(a-c)]. The difference $\zeta_s - \zeta_d > 0$ is analogous to the source−drain voltage in electronic devices. Whereas electrons are Fermions, IXs behave as bosons. This makes our transport problem unlike the electronic one. The problem is also different from the slit diffraction of photons or other bosons, such as phonons, considered so far. Indeed, one cannot apply a source−drain voltage to photons or phonons in any usual sense. (However, quantized *heat* transport of phonons[17−19] has been studied.)

To highlight the qualitative features, we do our numerical calculations for the case where the drain side is empty, $\zeta_d = -\infty$. The conductance of the QPC can be described by the bosonic variant of the standard Landauer−Büttiker theory.[20] It predicts that the contribution of a given subband to the total conductance can exceed N/h if its Bose−Einstein occupation factor is larger than unity.[21] To the best of our knowledge, there have been no direct experimental probes of this prediction in bosonic systems. The closest related experiment is probably the study of ^{6}Li atoms passing through a QPC in the regime of enhanced attractive interaction.[22] That experiment has demonstrated the conductance exceeding N/h, and the theory[23−25] has attributed this excess to the virtual pairing of Fermionic atoms into bosonic molecules by quantum fluctuations.

Below we present our theoretical results for the IX transport through single, double, and multiple QPCs. We ignore exciton−exciton interaction but comment on possible interaction effects at the end of the Letter.

Received: May 7, 2019
Revised: June 25, 2019
Published: July 2, 2019

ACS Publications © 2019 American Chemical Society

DOI: 10.1021/acs.nanolett.9b01877
Nano Lett. 2019, 19, 5373−5379

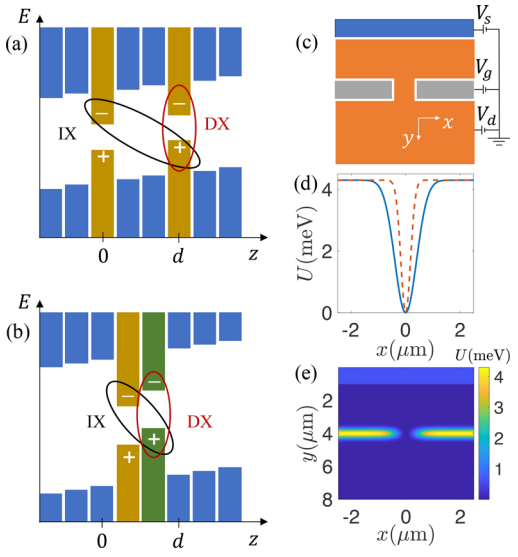

Figure 1. (a) Schematic energy band diagrams of an atomically thin electron−hole bilayer subject to an external electric field. The direct exciton (DX) is indicated by the red oval, the indirect exciton (IX) by the black one. The bars represent atomic planes. (b) Same as (a) for a spacer-free type II heterostructure. Various combinations of 2D materials can be used, examples include: For GaAs structures, GaAs (green), AlAs (yellow), and AlGaAs (blue); for TMD type I structures, MoS_2 (yellow) and hBN (blue); for TMD type II structures, WSe_2 (green), $MoSe_2$ (yellow), and hBN (blue). (c) Schematic of an IX QPC device. Voltage V_s (V_d) controls the electrochemical potential of the source (drain); V_g creates a potential constraining IXs from the sides. (d) Variation of the IX potential along the line $y = y_0$ across the QPC for a_x = 180 and 400 nm (dashed and solid trace, respectively) with other parameters as follows: A = 4.30 meV, C = 1, a_y = 200 nm, U_{sd} = 1.0 meV, y_0 = 4.0 μm, and y_1 = 1.0 μm; see eq 1. (e) False color map of $U(x,y)$ for the larger a_x in (d).

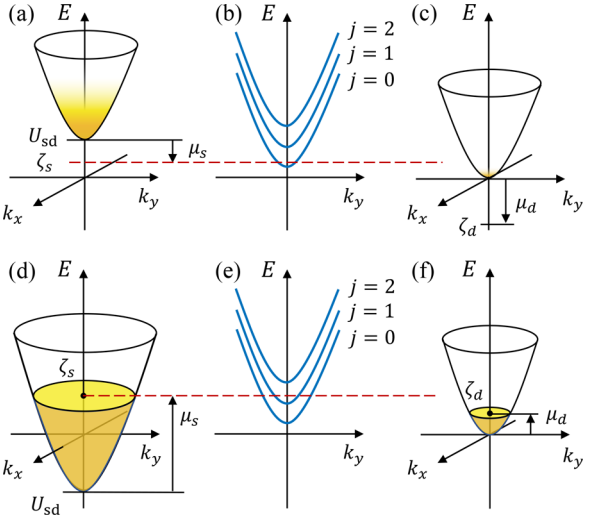

Figure 2. Energy spectra at the source (a, d), the QPC (b, e), and the drain (c, f). The electrochemical potential of the source is indicated by the horizontal dashed line. The shading represents the occupation factor. Panels (a−c) are for bosonic particles, such as IXs. Panels (d−f) are for Fermions, for example, electrons.

Model of a QPC. In the absence of external fields, the IXs are free to move in a two-dimensional (2D) x−y plane. When an external electric field $E_z = E_z(x,y)$ is applied in the z-direction (Figure 1a), an IX experiences the energy shift $U = -eE_z d$. This property makes it possible to create desired external potentials $U(x,y)$ acting on the IXs. To engineer a QPC, $U(x,y)$ needs to have a saddle-point shape. Such a potential can be created using a configuration of electrodes: a global bottom gate plus a few local gates on top of the device.

As depicted in Figure 1b, two of such top electrodes (gray) can provide the lateral confinement, and another two (blue and orange) can control the potential at the source and the drain. More electrodes can be added if needed. Following previous work,[11] in our numerical simulations we use a simple model for $U(x,y)$:

$$U(x, y) = A(1 - Ce^{-x^2/2a_x^2})e^{-(y-y_0)^2/2a_y^2} + U_{sd}f_F\left(\frac{y - y_1}{s}\right) \quad (1)$$

where $f_F(x) = (e^x + 1)^{-1}$ is the Fermi function. The width parameters a_x and a_y and the coefficients A and C on the first line of eq 1 are tunable by the gate voltage V_g (Figure 1b). The second line in eq 1 represents a gradual potential drop of magnitude U_{sd}, central coordinate y_1, and a characteristic width s in the y-direction. These parameters are controlled by voltages V_s and V_d. Examples of $U(x,y)$ are shown in Figure 1c,d.

For qualitative discussions, we also consider the model of a quasi-1D channel of a long length L_c and a parabolic confining potential. The corresponding $U(x,y)$ is obtained by replacing the top line of eq 1 with

$$f_F\left(\frac{y_0 - L_c - y}{s}\right)f_F\left(\frac{y - y_0}{s}\right)\left(U_0 + \frac{1}{2}U_{xx}x^2\right) \quad (2)$$

where $U_{xx} = AC/a_x^2$. The energy subbands (Figure 2b) in such a channel are

$$E_j(k_y) = U_0 + \hbar\omega_x\left(j + \frac{1}{2}\right) + \frac{\hbar^2 k_y^2}{2m}, \quad j = 0, 1, \ldots \quad (3)$$

The associated eigenstates are the products of the plane waves $e^{ik_y y}$ and the harmonic oscillator wave functions

$$\chi_j(x) = H_j(\sqrt{2}x/w_0)\exp(-x^2/w_0^2) \quad (4)$$

where $H_j(x)$ is the Hermite polynomial of degree j. The length w_0 and frequency ω_x are given by

$$w_0 = \sqrt{\frac{2\hbar}{m\omega_x}}, \quad \omega_x = \sqrt{\frac{U_{xx}}{m}} \quad (5)$$

The subband energy spacing $\hbar\omega_x$ can be estimated as

$$\hbar\omega_x \simeq 8.8\,\text{meV}\left(\frac{m_0}{m}\right)^{1/2}\left(\frac{AC}{\text{meV}}\right)^{1/2}\left(\frac{\text{nm}}{a_x}\right) \quad (6)$$

which is approximately 0.1 meV for devices made of transition-metal dichalcogenides (TMDs), where exciton effective mass $m = 1.0m_0$ and a_x = 180 nm. Hence, the onset of quantization occurs at $T \sim 1$ K. The same characteristic energy scales in GaAs quantum well devices[11] can be obtained in a wider QPC, a_x = 400 nm, taking advantage of the lighter mass, $m = 0.2m_0$, compare solid and dashed lines in Figure 1d. In both examples $\hbar\omega_x$ is much smaller than the IX binding energy (~300 meV in TMDs[26] and ~4 meV in GaAs[27,28]). Therefore, we consider the approximation ignoring internal dynamics of the IXs as they pass through the QPC[29] and treat them as point-like

DOI: 10.1021/acs.nanolett.9b01877
Nano Lett. 2019, 19, 5373−5379

particles. Incidentally, we do not expect any significant reduction of the exciton binding energy due to many-body screening in the considered low-carrier-density regime in semiconductors with a sizable gap and no extrinsic doping. (At high carrier densities, the screening effect can be substantial.[30])

Conductance of a QPC. As with usual electronic devices, we imagine that our QPC is connected to a semi-infinite source and drain leads (labeled by $l = s,d$). Inside the leads the IX potential energy $U(x,y)$ tends to asymptotic values U_l. Without loss of generality, we can take $U_d = 0$, as in eq 1. The difference $U_{sd} = U_s - U_d = \alpha(eV_s - eV_d)$ is a linear function of the control voltages V_s, V_d (Figure 1b). The coefficient of proportionality can be estimated as $\alpha \sim d/d_g$, where d_g is the vertical distance between the top and bottom electrodes. The IX energy dispersions at the source and the drain are parabolic and are shifted by U_{sd} with respect to one another, see Figure 2a,c. In the experiment, the IX density of the reservoirs can be controlled by photoexcitation power. For example, the IX density n_s can be generated on the source side only,[11] while the drain side can be left practically empty, $n_d \ll n_s$. This is the case we focus on below. The chemical potentials μ_l are related to the densities n_l via[31,32]

$$\mu_l = T\ln(1 - e^{-T_0/T}), \qquad T_0 \equiv \frac{2\pi\hbar^2 n_l}{mN} \tag{7}$$

Note that we count the chemical potentials from the minima of the appropriate energy spectra and that we use the units system $k_B \equiv 1$. In turn, the electrochemical potentials are given by

$$\zeta_l = \mu_l + U_l \tag{8}$$

which implies

$$U_{sd} = (\zeta_s - \zeta_d) - (\mu_s - \mu_d) \tag{9}$$

In the terminology of electron devices, the first term in eq 9 is related to the source−drain voltage V_{sd}, namely, $\zeta_s - \zeta_d \equiv -eV_{sd}$. The second term in eq 9 is referred to as the built-in potential, which is said to originate from charge redistribution in the leads.

If the particle densities n_l are fixed, then variations of $\zeta_s - \zeta_d$ rigidly track those of U_{sd}. The differential conductance can be computed by taking the derivative of the source−drain particle current I with respect to U_{sd}:

$$G = (\partial I/\partial U_{sd})_{n_s,n_d} \tag{10}$$

G has a dimension of $1/h$ and its natural quantum unit is N/h. (The spin-valley degeneracy is $N = 4$ in both TMDs and GaAs.)

For the long-channel model (eq 2), G can be calculated analytically because the single-particle transmission coefficients through the QPC have the form $t_j(E) = \theta(E - E_j^0)$, that is, they take values of either 0 or 1. Here $E_j^0 \equiv E_j(0)$, and $\theta(x)$ is the Heaviside step-function. Adopting the standard Landauer−Büttiker theory for Fermions[20] to the present case of bosons (see also ref 21), we find the total current to be $I = \sum_j (I_{s,j} - I_{d,j})$, where the partial currents are

$$I_{a,j} = \frac{N}{h}\int_{U_a}^{\infty} f_B\left(\frac{E - \zeta_a}{T}\right) t_j(E)\,dE \tag{11}$$

and $f_B(x) = (e^x - 1)^{-1}$ is the Bose function. In turn, the conductance is

$$G = \frac{N}{h}\sum_j \theta(E_j^0 - U_{sd}) f_B\left(\frac{E_j^0 - U_{sd} - \mu_s}{T}\right) \tag{12}$$

The dependence of G on U_{sd} is illustrated in Figure 3a. The conductance exhibits asymmetric peaks. Each peak signals the activation of a new conduction channel whenever U_{sd} approaches the bottom of a particular 1D subband. All the peaks have the same shape, which is the mirror-reflected Bose function with a sharp cutoff. As T decreases, the width of the peaks $\Delta \sim \min(T, -\mu_s)$ decreases. The magnitude of the peaks $G_{max} = (N/h) f_B(-\mu_s/T)$ can be presented in the form:

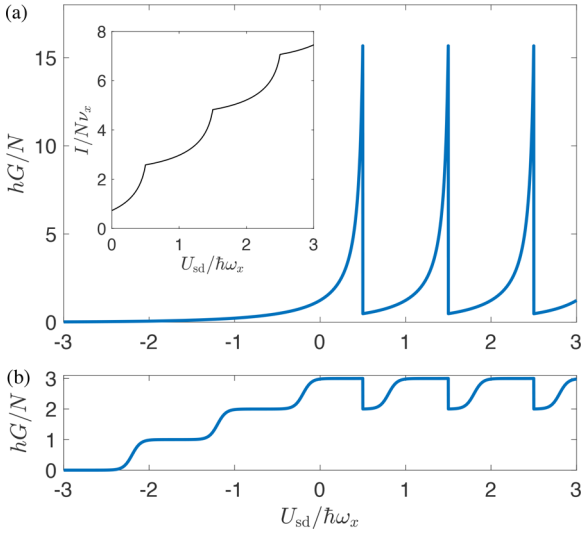

Figure 3. (a) Conductance of a bosonic QPC vs U_{sd} from the adiabatic approximation (eq 12) for $T = 0.8\hbar\omega_x$, $\mu_s = -0.05\hbar\omega_x$. Inset: Total current as a function of U_{sd}. The notation used on the y-axis is $\nu_x \equiv \omega_x/2\pi$. (b) Conductance of a Fermionic QPC for $T = 0.05\hbar\omega_x$, $\mu_s = 2.7\hbar\omega_x$. Note that the number of conductance steps occurring at $U_{sd} < E_0^0 = \frac{1}{2}\hbar\omega_x$ is equal to $\mu_s/\hbar\omega_x$ rounded up to the nearest integer.

$$G_{max} = \frac{N}{h} f_{max} \tag{13}$$

where f_{max} is the occupation of the lowest energy state at the source. For Fermions, f_{max} is limited by 1. For 2D bosons, $f_{max} = e^{T_0/T} - 1$ exceeds 1, and, in turn, G_{max} exceeds N/h at $T < T_0/\ln 2$.

The sudden drops of G at $U_{sd} = E_j^0$ (Figure 3a) occur because the current carried by each subband saturates as soon as it becomes accessible to all the IXs injected from the source, down to the lowest energy U_{sd}. These constant terms do not affect the differential conductance G. The total current as a function of U_{sd} is plotted in the inset of of Figure 3a.

It is again instructive to compare these results with the more familiar ones for Fermions, which are obtained replacing the Bose function f_B with the Fermi function f_F in eq 12. In the regime where U_{sd} is large and negative, the Heaviside functions in eq 12 play no role, so that G traces the expected quantized staircase shown in Figure 3b. The conductance steps occur whenever $U_{sd} = E_j^0 - \mu_s$. Once U_{sd} approaches $E_0^0 = \hbar\omega_x/2$, a different behavior is found: The conductance displays additional sudden drops at $U_{sd} = E_j^0$, which causes it to oscillate between two quantized values. These drops appear for

DOI: 10.1021/acs.nanolett.9b01877
Nano Lett. 2019, 19, 5373−5379

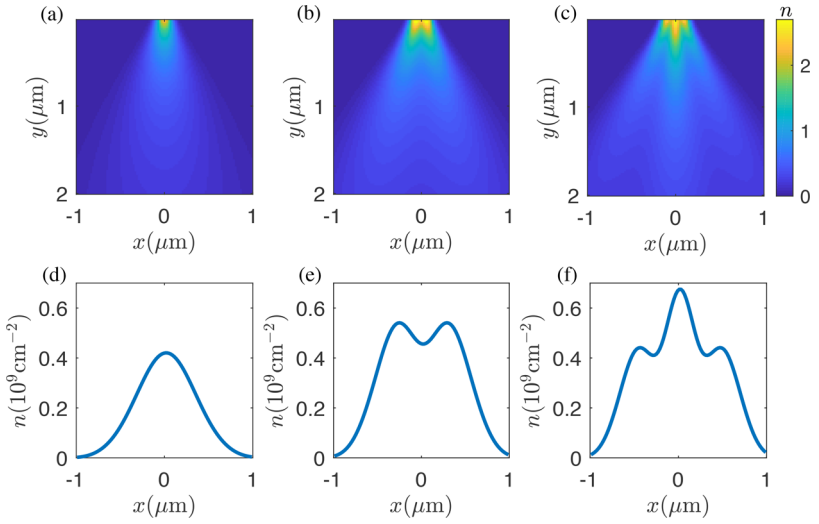

Figure 4. IX density distribution in a QPC for three different U_{sd}. Panels (a–c) depict the density distribution n in the x–y plane in units of 10^9 cm^{-2}. Panels (d–f) show the profiles of n along the midline, $y = 1$ μm, of the region plotted directly above. Values of U_{sd} are adjusted to highlight the contributions of particular subbands: (a, d) $j = 0$ for $U_{sd} = 0.52$, (b, e) $j = 1$ for $U_{sd} = 1.52$, (c, f) $j = 2$ for $U_{sd} = 2.52$, all in units of $\hbar\omega_x = 0.10$ meV; $T = 1.0$ K everywhere.

the same reason as in the bosonic case: current saturation for each subband that satisfies the condition $E_j^0 < U_{sd}$.

The adiabatic QPC model considered above is often a good approximation[12,13] for more realistic models, such as eq 1. The latter cannot be treated analytically but we were able to compute G numerically, using the transfer matrix method[33] (see below). The results are presented in the Supporting Information. The main difference from the adiabatic case is that the conductance peaks are reduced in magnitude and broadened.

Density Distribution in a QPC. In analogy to experiments with electronic QPCs,[15] it would be interesting to study quantized conduction channels by the optical imaging of IX flow. Unlike electrons, IXs can recombine and emit light, so that the IX photoluminescence can be used for measuring their current paths. This motivates us to model the density distribution $n(x,y)$ of IXs in the QPC. We begin with analytical considerations and then present our numerical results (Figure 4).

The calculation of the $n(x,y)$ involves two steps. First, we solve the Schrödinger equation for the single-particle energies $E = \hbar^2 k'^2/(2m)$ and the wave functions $\psi(x,y)$ of IXs subject to the potential $U(x,y)$. The boundary conditions for the $\psi(x,y)$ is to approach linear combinations of plane waves of momenta $\mathbf{k}' = (k_x', \pm k_y')$ at $y \to -\infty$ but contain no waves of momenta $\mathbf{k}'' = (k_x'', k_y'')$ with $\mathrm{Re}\, k_y'' < 0$ at $y \to +\infty$. Such states correspond to waves incident from the source. Second, we sum the products $f_B(E - \zeta_s)|\psi(x,y)|^2$ to obtain the $n(x,y)$. We choose not to multiply the result by N, so that our $n(x,y)$ is the IX density per spin per valley.

For a qualitative discussion, let us concentrate on the simplest case of large k_y', that is, fast particles. As the incident wave propagates from the source lead, it first meets the smooth potential drop U_{sd} at $y = y_1$. Assuming $k_y's \gg 1$, the over-the-barrier reflection at $y = y_1$ can be neglected. Therefore, the y momentum increases to the value k_y dictated by the energy conservation:

$$k_y^2 = k_y'^2 + (2m/\hbar^2)U_{sd} \tag{14}$$

while the x momentum k_x' remains the same. Subsequently, the incident wave impinges on the QPC at $y = y_0$. Typically, this causes a strong reflection back to the source. However, certain eigenstates have a non-negligible transmission. After passing the QPC, their wave functions expand laterally with the characteristic angular divergence of $1/(k_y w_0) \ll 1$. Such wave functions can be factorized $\psi(x, y) = e^{ik_y y}\chi(x, y)$, where the slowly varying amplitude $\chi(x,y)$ obeys the eikonal (or paraxial) equation:

$$\left(-i\hbar v_y \partial_y - \frac{\hbar^2}{2m}\partial_x^2 + U\right)\chi = 0, \qquad v_y \equiv \frac{\hbar k_y}{m} \tag{15}$$

If the model of the long constriction (eq 2) is a good approximation, the solution is as follows. Inside the QPC, $\chi(\mathbf{r})$ is proportional to a particular oscillator wave function $\chi_j(x)$ (eq 4). Outside the QPC, it behaves as a Hermite-Gaussian beam whose probability density can be written in the scaling form

$$|\chi(x, y)|^2 = \frac{1}{b(y)}\chi_j^2\left(\frac{x}{b(y)}\right) \tag{16}$$

$$b(y) = \sqrt{1 + \frac{(y - y_0)^2}{w_y^2}} \tag{17}$$

$$w_y = \frac{1}{2}k_y w_0^2 \tag{18}$$

This representation has been used in the study of a Bose–Einstein condensate (BEC) expansion from a harmonic trap.[34,35] Our problem of the steady-state 2D transport through the QPC maps to the non-interacting limit of this problem in 1 + 1D, with $t = (y - y_0)/v_y$ playing the role of time. In other words, the IX current emerging from the QPC is mathematically similar to a freely expanding BEC. This mapping is accurate if the characteristic width of the energy distribution of the IX injected into the QPC from the source is small enough, $\Delta \ll \hbar\omega$. Dimensionless function $b(y)$ has the meaning of the expansion factor. A salient feature of the eigenfunctions is the nodal lines $\chi(x,y) = 0$. The lowest

DOI: 10.1021/acs.nanolett.9b01877
Nano Lett. 2019, 19, 5373–5379

subband $j = 0$ has no such lines, whereas the higher subbands have exactly $j = 1, 2, \ldots$ of them.

For a quantitative modeling, we carried out simulations using the transfer matrix method.[33] This method gives a numerical solution of the Schrödinger equation discretized on a finite-size real-space grid for a given energy E and the boundary conditions described above. To obtain the total particle density, we summed the contributions of individual states, making sure to include enough E's to achieve convergence. In all of our calculations, the chemical potential μ_s was fixed to produce the density (per spin per valley) $n_s = 1.0 \times 10^{10}$ cm^{-2} at the source. Examples of such calculations for temperature $T = 1.0$ K are shown in Figure 4. Since the partial densities $|\psi(x,y)|^2$ are weighted with the Bose–Einstein factor $f_B(E - \zeta_s)$, the lowest-energy $j = 0$ subband typically dominates the total density, making it look like a nodeless Gaussian beam (Figure 4a,d). However, if U_{sd} is tuned slightly above the bottom of the $j = 1$ subband, the contribution of this subband is greatly enhanced by the van Hove singularity of the 1D density of states $N/(\pi\hbar v_y) \propto$ (inside the QPC. As a result, $n(x,y)$ develops a valley line (local minimum) at $x = 0$, which is the nodal line of function $\chi_1(x/b,y)$ (Figure 4b,e). A similar phenomenon occurs when we tune U_{sd} to slightly above the bottom of $j = 2$ subband. Here the density exhibits two valley lines, which approximately follow the nodal lines of function $\chi_2(x/b,y)$ (Figure 4c,f). These theoretical predictions may be tested by imaging IX emission with high enough optical resolution. Note that these van Hove singularities do not enhance the differential conductivity G because of the cancellation between the density of states and the particle velocity v_y. As explained above, this leads to current saturation and thus a negligible contribution of jth subband to G at $U_{sd} > E_j^0$.

Double and Multiple QPC Devices. We have next explored the exciton analog of the Young double-slit interference. A short distance downstream from the first QPC (1.0 μm along y), we added another potential barrier constructed from two copies of the single-QPC potential (eq 1) shifted laterally in x. As in Young's classical setup, the first QPC plays the role of a coherent source for the double-QPC. An example of the latter with the center-to-center separation of 800 nm is shown in Figure 5a. We computed the IX density distribution in this system for U_{sd} at which the IXs fluxes through all of the QPCs that are dominated by the $j = 0$ subband. The IXs transmitted through the double-QPC create distinct interference fringes (Figure 5b,c).

Finally, we considered a four-QPC array. To show the results more clearly, we simulated the zero-temperature limit, where a single energy E contributes. As illustrated by Figure 6a, the interference pattern begins to resemble that of a diffraction grating. Near the QPCs, it exhibits the periodic refocusing known as the Talbot effect. The repeat distance for the complete refocusing is[36]

$$y_T = \frac{\lambda}{1 - \sqrt{1 - \frac{\lambda^2}{a^2}}} \tag{19}$$

where $\lambda = 2\pi/k_y$ is the de Broglie wavelength of the IXs and a is the distance between the QPCs. For $\lambda = 100$ nm and $a = 1000$ nm, this distance $y_T \simeq 20$ μm is beyond the range plotted in Figure 6a. Therefore, only the so-called fractional Talbot effect is seen in that figure. Although too fine for conventional imaging, these features may in principle be resolved by near-field optical techniques. Note that for a grating with N_s slits, the crossover to the far-field diffraction occurs at the distance $\sim N_s y_T$, which is prohibitively large for the transfer matrix simulations. For a qualitative illustration of this crossover, we computed the interference pattern simply by adding a number of Gaussian beams; see Figure 6b,c.

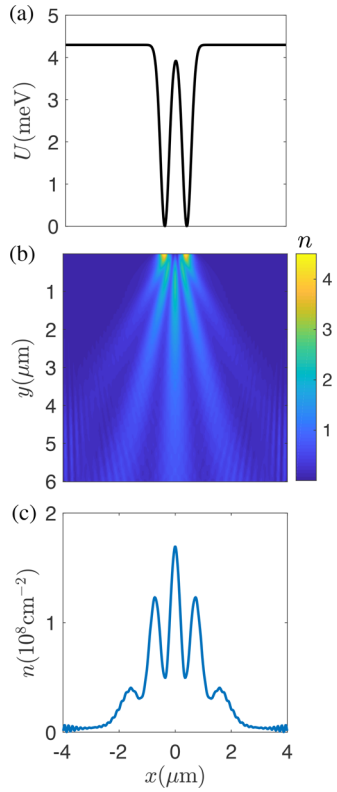

Figure 5. Double-QPC IX device. (a) The profile of the IX potential across the two constrictions. (b) The IX density in units of 10^8 cm^{-2}. (c) The IX density along the line $y = 2$ μm in (b). The ripples at the flanks of the fringes are finite-size artifacts.

Discussion and Outlook. In this Letter, we considered a few prototypical examples of mesoscopic IX phenomena. We analyzed the subband quantization of IX transport through a single QPC, the double-slit interference from two QPCs, and the Talbot effect in multiple QPCs. As for electrons, these phenomena should be experimentally observable at low enough temperatures. The present theory may be straightforwardly expanded to more complicated potential landscapes and structures.

In the present work, we neglected IX interactions. This interaction is dipolar, which in 2D is classified as short-range, parametrized by a certain interaction constant g. As mentioned above, the problem of the IX transport through a QPC is closely related to the problem of a BEC expansion from a harmonic trap. Following the studies of the latter,[34] interaction can be included at the mean-field level by using the Gross–Pitaevskii equation instead of the Schrödinger one. For the single-QPC case, we expect the GPE solution to show a faster lateral expansion of the exciton "jet", that is, a more rapid growth of function $b(y)$. For the double- and multi-QPC cases, we expect repulsive interaction to suppress the interference fringes, similar to what is observed in experiments with cold atoms.[38] The line shape and amplitude (visibility) of the fringes remain to be investigated.

DOI: 10.1021/acs.nanolett.9b01877
Nano Lett. 2019, 19, 5373–5379

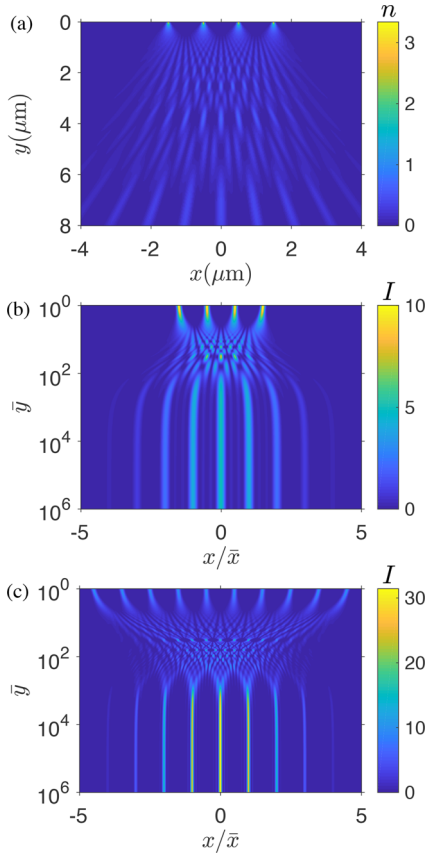

Figure 6. False color maps illustrating IX density in multiple QPC systems. (a) Talbot-like interference in a four-QPC device. The incident beam consists of a single plane wave, corresponding to the $T = 0$ limit. $U_{sd} = 0.10$ meV. (b) Rescaled intensity $I \equiv |\psi(r)|^2 \bar{x}$ of the interference pattern of $N_s = 4$ Gaussian beams. Following an example in the literature,[37] the horizontal axis is normalized by $\bar{x} = (\lambda y/a) + a$ with $a = 1$ μm. The vertical axis represents $\bar{y} = (y/w_y) + 1$. (c) Same as (b) for $N_s = 10$.

Applications of our theory to real semiconductor systems would also require taking into account the spin and valley degrees of freedom of IXs. It would be interesting to study spin transport of IXs[5,9,10] through nanoconstrictions and associated spin textures. This could be an alternative pathway to probing spin conductance of quasi-1D channels.[39]

The field of mesoscopic exciton systems is currently in its infancy, but it is positioned to grow, extending the phenomena studied in voltage-controllable electron systems to bosons. More importantly, it has the potential to reveal brand new phenomena. There are many intriguing subjects for future work.

■ ASSOCIATED CONTENT

Supporting Information

The Supporting Information is available free of charge on the ACS Publications website at DOI: 10.1021/acs.nanolett.9b01877.

Electrostatic simulations of GaAs and TMD IX devices; derivation of eq 12; transport simulations by the transfer matrix method (PDF)

■ AUTHOR INFORMATION

Corresponding Author

*E-mail: chx035@ucsd.edu.

ORCID

Chao Xu: 0000-0003-3834-1452

Notes

The authors declare no competing financial interest.

■ ACKNOWLEDGMENTS

The work at UCSD is supported by the National Science Foundation under grant ECCS-1640173 and by the NERC, a subsidiary of Semiconductor Research Corporation through the SRC-NRI Center for Excitonic Devices.

■ REFERENCES

(1) Lozovik, Y. E.; Yudson, V. I. A new mechanism for superconductivity: pairing between spatially separated electrons and holes. *J. Exp. Theor. Phys.* **1976**, *44*, 389−397.

(2) Hagn, M.; Zrenner, A.; Böhm, G.; Weimann, G. Electric-field-induced exciton transport in coupled quantum well structures. *Appl. Phys. Lett.* **1995**, *67*, 232−234.

(3) Gärtner, A.; Holleitner, A. W.; Kotthaus, J. P.; Schuh, D. Drift mobility of long-living excitons in coupled GaAs quantum wells. *Appl. Phys. Lett.* **2006**, *89*, 052108.

(4) Hammack, A. T.; Butov, L. V.; Wilkes, J.; Mouchliadis, L.; Muljarov, E. A.; Ivanov, A. L.; Gossard, A. C. Kinetics of the inner ring in the exciton emission pattern in coupled GaAs quantum wells. *Phys. Rev. B: Condens. Matter Mater. Phys.* **2009**, *80*, 155331.

(5) Leonard, J. R.; Kuznetsova, Y. Y.; Yang, S.; Butov, L. V.; Ostatnicky, T.; Kavokin, A.; Gossard, A. C. Spin transport of excitons. *Nano Lett.* **2009**, *9*, 4204−4208.

(6) Lazić, S.; Santos, P.; Hey, R. Exciton transport by moving strain dots in GaAs quantum wells. *Phys. E* **2010**, *42*, 2640−2643.

(7) Alloing, M.; Lemaître, A.; Galopin, E.; Dubin, F. Nonlinear dynamics and inner-ring photoluminescence pattern of indirect excitons. *Phys. Rev. B: Condens. Matter Mater. Phys.* **2012**, *85*, 245106.

(8) Lazić, S.; Violante, A.; Cohen, K.; Hey, R.; Rapaport, R.; Santos, P. Scalable interconnections for remote indirect exciton systems based on acoustic transport. *Phys. Rev. B: Condens. Matter Mater. Phys.* **2014**, *89*, 085313.

(9) Finkelstein, R.; Cohen, K.; Jouault, B.; West, K.; Pfeiffer, L. N.; Vladimirova, M.; Rapaport, R. Transition from spin-orbit to hyperfine interaction dominated spin relaxation in a cold fluid of dipolar excitons. *Phys. Rev. B: Condens. Matter Mater. Phys.* **2017**, *96*, 085404.

(10) High, A. A.; Leonard, J. R.; Hammack, A. T.; Fogler, M. M.; Butov, L. V.; Kavokin, A. V.; Campman, K. L.; Gossard, A. C. Spontaneous coherence in a cold exciton gas. *Nature* **2012**, *483*, 584.

(11) Dorow, C.; Leonard, J.; Fogler, M.; Butov, L.; West, K.; Pfeiffer, L. Split-gate device for indirect excitons. *Appl. Phys. Lett.* **2018**, *112*, 183501.

(12) Wharam, D. A.; Thornton, T. J.; Newbury, R.; Pepper, M.; Ahmed, H.; Frost, J. E. F.; Hasko, D. G.; Peacock, D. C.; Ritchie, D. A.; Jones, G. A. C. One-dimensional transport and the quantisation of the ballistic resistance. *J. Phys. C: Solid State Phys.* **1988**, *21*, L209.

(13) Van Wees, B.; Van Houten, H.; Beenakker, C.; Williamson, J. G.; Kouwenhoven, L.; Van der Marel, D.; Foxon, C. Quantized conductance of point contacts in a two-dimensional electron gas. *Phys. Rev. Lett.* **1988**, *60*, 848.

(14) Micolich, A. Double or nothing? *Nat. Phys.* **2013**, *9*, 530−531.

(15) Topinka, M.; LeRoy, B.; Shaw, S.; Heller, E.; Westervelt, R.; Maranowski, K.; Gossard, A. Imaging coherent electron flow from a quantum point contact. *Science* **2000**, *289*, 2323−2326.

(16) Krinner, S.; Stadler, D.; Husmann, D.; Brantut, J.-P.; Esslinger, T. Observation of quantized conductance in neutral matter. *Nature* **2015**, *517*, 64.

DOI: 10.1021/acs.nanolett.9b01877
Nano Lett. 2019, 19, 5373−5379

(17) Schwab, K.; Henriksen, E.; Worlock, J.; Roukes, M. L. Measurement of the quantum of thermal conductance. *Nature* **2000**, *404*, 974.
(18) Gotsmann, B.; Lantz, M. A. Quantized thermal transport across contacts of rough surfaces. *Nat. Mater.* **2013**, *12*, 59.
(19) Cui, L.; Jeong, W.; Hur, S.; Matt, M.; Klöckner, J. C.; Pauly, F.; Nielaba, P.; Cuevas, J. C.; Meyhofer, E.; Reddy, P. Quantized thermal transport in single-atom junctions. *Science* **2017**, *355*, 1192−1195.
(20) Büttiker, M.; Imry, Y.; Landauer, R.; Pinhas, S. Generalized many-channel conductance formula with application to small rings. *Phys. Rev. B: Condens. Matter Mater. Phys.* **1985**, *31*, 6207−6215.
(21) Papoular, D.; Pitaevskii, L.; Stringari, S. Quantized conductance through the quantum evaporation of bosonic atoms. *Phys. Rev. A: At., Mol., Opt. Phys.* **2016**, *94*, 023622.
(22) Krinner, S.; Lebrat, M.; Husmann, D.; Grenier, C.; Brantut, J.-P.; Esslinger, T. Mapping out spin and particle conductances in a quantum point contact. *Proc. Natl. Acad. Sci. U. S. A.* **2016**, *113*, 8144−8149.
(23) Kanász-Nagy, M.; Glazman, L.; Esslinger, T.; Demler, E. A. Anomalous Conductances in an Ultracold Quantum Wire. *Phys. Rev. Lett.* **2016**, *117*, 255302.
(24) Uchino, S.; Ueda, M. Anomalous Transport in the Superfluid Fluctuation Regime. *Phys. Rev. Lett.* **2017**, *118*, 105303.
(25) Liu, B.; Zhai, H.; Zhang, S. Anomalous conductance of a strongly interacting Fermi gas through a quantum point contact. *Phys. Rev. A: At., Mol., Opt. Phys.* **2017**, *95*, 013623.
(26) Latini, S.; Winther, K. T.; Olsen, T.; Thygesen, K. S. Interlayer Excitons and Band Alignment in MoS_2 /hBN/WSe_2 van der Waals Heterostructures. *Nano Lett.* **2017**, *17*, 938−945.
(27) Szymanska, M. H.; Littlewood, P. B. Excitonic binding in coupled quantum wells. *Phys. Rev. B: Condens. Matter Mater. Phys.* **2003**, *67*, 193305.
(28) Sivalertporn, K.; Mouchliadis, L.; Ivanov, A. L.; Philp, R.; Muljarov, E. A. Direct and indirect excitons in semiconductor coupled quantum wells in an applied electric field. *Phys. Rev. B: Condens. Matter Mater. Phys.* **2012**, *85*, 045207.
(29) Grasselli, F.; Bertoni, A.; Goldoni, G. Exact two-body quantum dynamics of an electron-hole pair in semiconductor coupled quantum wells: A time-dependent approach. *Phys. Rev. B: Condens. Matter Mater. Phys.* **2016**, *93*, 195310.
(30) Kharitonov, M. Y.; Efetov, K. B. Electron screening and excitonic condensation in double-layer graphene systems. *Phys. Rev. B: Condens. Matter Mater. Phys.* **2008**, *78*, 241401.
(31) Remeika, M.; Leonard, J. R.; Dorow, C. J.; Fogler, M. M.; Butov, L. V.; Hanson, M.; Gossard, A. C. Measurement of exciton correlations using electrostatic lattices. *Phys. Rev. B: Condens. Matter Mater. Phys.* **2015**, *92*, 115311.
(32) Ivanov, A. L.; Littlewood, P. B.; Haug, H. Bose−Einstein statistics in thermalization and photoluminescence of quantum-well excitons. *Phys. Rev. B: Condens. Matter Mater. Phys.* **1999**, *59*, 5032−5048.
(33) Usuki, T.; Saito, M.; Takatsu, M.; Kiehl, R. A.; Yokoyama, N. Numerical analysis of ballistic-electron transport in magnetic fields by using a quantum point contact and a quantum wire. *Phys. Rev. B: Condens. Matter Mater. Phys.* **1995**, *52*, 8244−8255.
(34) Kagan, Y.; Surkov, E. L.; Shlyapnikov, G. V. Evolution of a Bose-condensed gas under variations of the confining potential. *Phys. Rev. A: At., Mol., Opt. Phys.* **1996**, *54*, R1753.
(35) Castin, Y.; Dum, R. Bose−Einstein condensates in time dependent traps. *Phys. Rev. Lett.* **1996**, *77*, 5315.
(36) Rayleigh, L. XXV. On copying diffraction gratings and some phenomena connected therewith. *Philos. Mag.* **1881**, *11*, 196−205.
(37) Juffmann, T.; Ulbricht, H.; Arndt, M. Experimental methods of molecular matter-wave optics. *Rep. Prog. Phys.* **2013**, *76*, 086402.
(38) Kohstall, C.; Riedl, S.; Sánchez Guajardo, E. R.; Sidorenkov, L. A.; Denschlag, J. H.; Grimm, R. Observation of interference between two molecular Bose−Einstein condensates. *New J. Phys.* **2011**, *13*, 065027.
(39) Meier, F.; Loss, D. Magnetization Transport and Quantized Spin Conductance. *Phys. Rev. Lett.* **2003**, *90*, 167204.

DOI: 10.1021/acs.nanolett.9b01877
Nano Lett. 2019, 19, 5373−5379

Supporting Information for Exciton Gas Transport Through Nano-Constrictions

Chao Xu,*,† Jason R. Leonard,† Chelsey J. Dorow,† Leonid V. Butov,† Michael M. Fogler,† Dmitri E. Nikonov,‡ and Ian A. Young‡

†*Department of Physics, University of California San Diego, 9500 Gilman Drive, La Jolla, California 92093, USA*

‡*Components Research, Intel Corporation, Hillsboro, Oregon 97124, USA*

Electrostatic simulations

To better assess the practicality of the proposed IX devices, we numerically modeled several systems of the type shown in Fig. 1(a) of the main text. The first example we considered is a TMD heterostructure with the following layer sequence. First, there is a thin crystal of hBN, which serves as both the encapsulating layer and the gate dielectric. Next, there are MoS_2 monolayers with two monolayers of hBN in between. Finally, there is a thicker hBN capping layer. Assuming the effective electron-hole separation d is equal to the center-to-center distance of the two MoS_2 layers and using 0.33 nm and 0.65 nm for the inter-layer spacing of, respectively, hBN and MoS_2, we get $d = 1.31$ nm in this design. We took the thickness of the lower hBN layer to be 10 nm, corresponding to about 30 atomic layers, and the total thickness of the structure to be $d_g = 175$ nm. The structure is assumed to reside on a ground plane, e.g., a graphite substrate, and to possess a set of top gates depicted in Fig. 1(c) of the main text. Specifically, two symmetrically placed slits shaped as square hairpins (⊐ and ⊏), divide the top plane into two rectangular side gates maintained at voltage V_g plus a narrow-necked central gate kept at voltage V_d.

To compute the electrostatic potential distribution in this system we used a commercial finite-element solver.[1] Note that both hBN and MoS_2 are materials with anisotropic permittivities[2] $\epsilon_{x\text{-}y,\,\mathrm{hBN}} = 6.71$, $\epsilon_{z,\,\mathrm{hBN}} = 3.56$ and $\epsilon_{x\text{-}y,\,\mathrm{MoS_2}} = 14.29$, $\epsilon_{z,\,\mathrm{MoS_2}} = 6.87$. To simplify the simulations, we assigned MoS_2 the same permittivities as hBN. In doing so, neglecting the difference of the in-plane permittivities is justified because the IX potential $U(x,y)$ is determined by the E_z-field. However, it is necessary to account for the difference of the z-axis permittivities, which we did by multiplying the calculated $U(x,y)$ by the factor

$$H + (1-H)\frac{\epsilon_{z,\,\mathrm{hBN}}}{\epsilon_{z,\,\mathrm{MoS_2}}} = 1.46\,. \tag{S1}$$

Here $H = 0.66\,\mathrm{nm}/d = 0.50$ is the fraction of the distance d occupied by the hBN spacer. We found that a reasonably close fit to $U(x,y)$ plotted by the dashed line in Fig. 1(d) of the main text can be achieved if the width of the side gates is 100 nm, the width of the slits is 100 nm as well, and the width of the neck of the central gate is 500 nm. Such dimensions are attainable with standard nanofabrication methods. The applied voltages need to be $V_d = 4.1$ V on the central gate and $V_g = 3.8$ V on the side gates.

The second example we studied is an GaAs/AlGaAs heterostructure composed of 100 nm of undoped AlGaAs, followed by two 8-nm-thick GaAs quantum wells separated by a 4-nm-thick AlGaAs barrier, capped by another undoped AlGaAs layer to the total thickness of $d_g = 500$ nm. The center-to-center quantum well distance in this case is $d = 12$ nm. The usual choice of the bottom electrode is an n^+-GaAs substrate. We treated both GaAs and AlGaAs as isotropic materials with identical permittivity of $\epsilon = 12.5$. We found that the potential shown by the solid line in Fig. 1(d) can be realized for the following electrode dimensions: width 300 nm, slit width 200 nm, central neck width 1100 nm. The applied voltages are $V_d = 2.00$ V and $V_g = 1.85$ V. Realizing this design again appears to be a straightforward task.

Finally, we simulated the potential produced in the same GaAs/AlGaAs heterostructure by a different top electrode pattern, in which the slits delineating the side electrodes are curved, Fig. S1(a). The computed $U(x,y)$ is plotted in Fig. S1(b). This design gives a better approximation to an ideal adiabatic QPC, see below.

Derivation of Eq. (12)

The quasiparticle velocity of jth subband is

$$v_j(k_y) = \frac{1}{\hbar}\frac{dE_j}{dk_y}\,. \tag{S2}$$

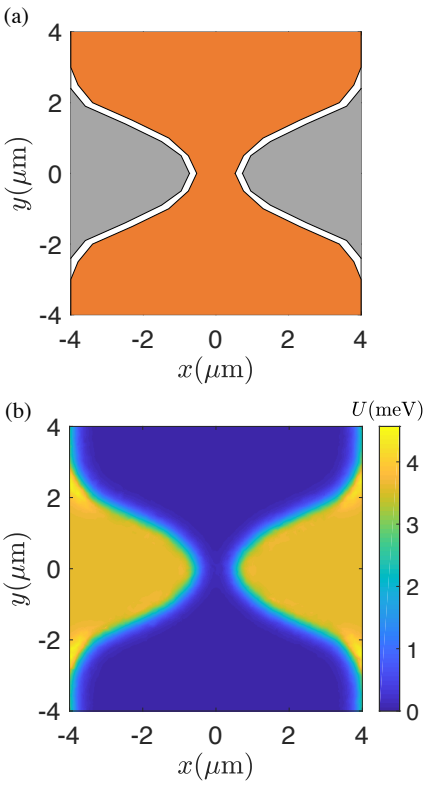

Figure S1. An example of simulated QPC devices. (a) top gate geometry (b) IX potential $U(x,y)$. In the proposed GaAs device (see text), this potential is realized for applied voltages $V_d = 2.00\,\mathrm{V}$ and $V_g = 1.85\,\mathrm{V}$.

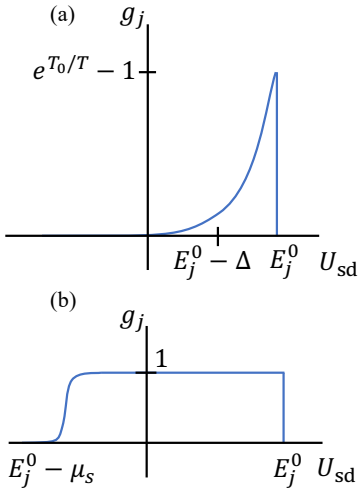

Figure S2. Dimensionless differential conductance of a single subband j of a long (adiabatic) QPC: (a) bosonic case, $\Delta = \min(T, -\mu_s)$. (b) fermionic case.

Therefore, the current injected by the source into the subband j is

$$I_{s,j} = N \int_0^\infty t_j(E_j) f_{B,F}(E_j - \zeta_s)\theta(E_j - U_{\mathrm{sd}}) v_j(k_y) \frac{dk_y}{2\pi}$$
$$= \frac{N}{h} \int_{U_{\mathrm{sd}}}^\infty t_j(E) f_{B,F}(E - \zeta_s) dE\,, \tag{S3}$$

which agrees with Eq. (11) of the main text. Here B, F label the bosonic and fermionic cases, respectively. The current $I_{d,j}$ injected by the drain is computed similarly. For an adiabatic QPC with the transmission coefficients $t_j(E) = \theta(E - E_j^0)$, the net current $I_j = I_{s,j} - I_{d,j}$ of jth subband is

$$I_j = \frac{N}{h} \int_{U_{\mathrm{sd}}}^\infty \theta(E - E_j^0) f_{F,B}(E - U_{\mathrm{sd}} - \mu_s) dE$$
$$- \frac{N}{h} \int_0^\infty \theta(E - E_j^0) f_{F,B}(E - \mu_d) dE\,. \tag{S4}$$

Accordingly, the differential conductance defined by Eq. (10) of the main text can be written as

$$G = \sum_j \partial I_j / \partial U_{\mathrm{sd}} = (N/h) \sum_j g_j\,, \tag{S5}$$

where

$$g_j = \theta(E_j^0 - U_{\mathrm{sd}}) f_{F,B}(E_j^0 - U_{\mathrm{sd}} - \mu_s) \tag{S6}$$

is the dimensionless conductance of subband j. This quantity depends on U_{sd} the same way as the mirror-reflected quasiparticle occupation factor $f_{B,F}$ until U_{sd} reaches E_j^0, at which point g_j drops to zero, see Fig. S3. As explained in the main text, the reason for this cutoff behavior is that the current contributed by channel j remains constant if U_{sd} increases past the subband bottom E_j^0. Therefore, it does not affect the differential conductance. However, if the QPC is not perfectly adiabatic, the transmission coefficient $t_j(E)$ has a gradual rather than the sharp onset at E_j^0, and so the cutoff of g_j at $U_{\mathrm{sd}} = E_j^0$ is also gradual (see below). Finally, summing over all the subbands, we obtain the total differential conductance shown in Fig. 3 of the main text.

Transport simulations

To calculate the conductance of a bosonic QPC, we used the transfer matrix method.[3] In this method the 2D Schrödinger equation with energy E and potential $U(x,y)$ in the simulation region $-L/2 < x,y < L/2$ is represented by a tight-binding model on a square lattice with a suitably small lattice constant l. We take $L = 8\,\mu\mathrm{m}$ and $l = 20\,\mathrm{nm}$, giving us a simulation grid

with $N_x = 400$ points along the x-axis. The boundary conditions for the Schrödinger equation correspond to semi-infinite leads inside which the particles are subject to y-independent potentials

$$U_s(x) = U(x, -L/2)\,, \quad U_d(x) = U(x, +L/2)\,, \quad \text{(S7)}$$

for the source and the drain, respectively. The energy spectrum of the source lead consists of N_x subbands with dispersion $E_i^s + E_k$. Here E_i^s are the quantized energies of motion in the potential $U_s(x)$,

$$E_k = \frac{\hbar^2}{ml^2}(1 - \cos kl), \quad \text{(S8)}$$

is the kinetic energy of the y-motion, and k is the y-axis momentum. The y-axis velocity is

$$u_i(E_k) = \frac{1}{\hbar}\frac{dE_k}{dk} = \sqrt{\frac{2E_k}{m}\left(1 - \frac{ml^2}{2\hbar^2}E_k\right)}\,. \quad \text{(S9)}$$

Similar energy spectrum exists in the drain. The transfer matrix algorithm computes the $N_x \times N_x$ matrix of the transmission coefficients $t_{ij}(E)$ between every subband i of the source and every subband j of the drain. To reduce the computation load, we did not explicitly include the potential drop $U_{\rm sd}$ in $U(x, y)$. As explained in the main text, this drop simply changes the particle velocity. We accounted for it by including the ratio of velocities before and after the drop as a multiplicative factor. Accordingly, our formula for the total current injected into the QPC by the subband i of the source is

$$I_i = \sum_k \frac{1}{L}\frac{u_i(E_k)}{u_i(E_k + U_{\rm sd})} f_B(E_k + E_i^s - \mu_s) \times \sum_j t_{ij}(E_k + E_i^s + U_{\rm sd}) u_j(E_k + U_{\rm sd})\,. \quad \text{(S10)}$$

The k-grid in the summation must be dense enough to achieve accuracy. We found the following choice adequate:

$$k = \frac{2\pi n}{L}, \quad n = 0, 1, \ldots, n_{\max} = \frac{L}{4l}\,. \quad \text{(S11)}$$

The net current through the QPC for the case of empty drain is simply $\sum_i I_i$.

For consistency check, consider first an ideal adiabatic QPC, where the transmission coefficients are $t_{ij}(E) = \delta_{ij}\theta(E - E_j^0)$. The rule for changing variables from k to k_y is found from the energy conservation

$$E_j(k_y) = E_k + E_i^s + U_{\rm sd}\,, \quad \text{(S12)}$$

which entails

$$\frac{1}{L}\sum_k \ldots \to \int \frac{dk_y}{2\pi}\frac{v_j(E)}{u_i(E_k)}\ldots \quad \text{(S13)}$$

Using these expressions, it is easy to see that Eq. (S10) is indeed transformed to Eq. (S3) in this limit. The corresponding analytical results for the current and conductance as functions of $U_{\rm sd}$ are plotted in Fig. S3 by the thick lines. Shown in the same Figure by the dashed lines are our numerical results for the potential of Fig. (S1)(b). They prove to be fairly close to the adiabatic limit except for some rounding of the conductance peaks and the current steps, as expected. On the other hand, the results for the potential $U(x, y)$ given by Eq. (1) of the main text, which are indicated by the thin lines, deviate more from the ideal case.

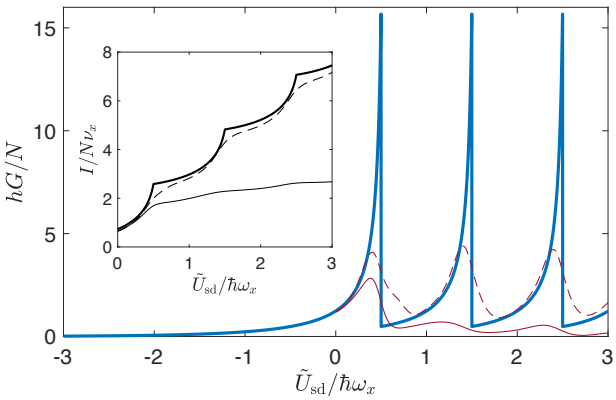

Figure S3. Conductance of a bosonic QPC as a function of electrostatic potential energy difference between the source and the QPC center $\tilde{U}_{\rm sd} \equiv U_{\rm sd} - U(0, y_0)$. The three lines correspond to three models considered: an ideal adiabatic constriction (thick line), a QPC with the potential of Fig. S1 (dashed line), a QPC defined by Eq. (1) of the main text (thin line). Inset: the total current vs. $\tilde{U}_{\rm sd}$ in these three models. Parameters: $T = 0.8\hbar\omega_x$, $\mu_s = -0.05\hbar\omega_x$.

References

(1) COMSOL Multiphysics® v. 4.0. http://www.comsol.com.

(2) Fogler, M. M.; Butov, L. V.; Novoselov, K. S. High-temperature superfluidity with indirect excitons in van der Waals heterostructures. *Nature Communications* **2014**, *5*, 4555.

(3) Usuki, T.; Saito, M.; Takatsu, M.; Kiehl, R. A.; Yokoyama, N. Numerical analysis of ballistic-electron transport in magnetic fields by using a quantum point contact and a quantum wire. *Physical Review B* **1995**, *52*, 8244–8255.